Mon. Not. R. Astron. Soc. **000**, 000–000 (0000) Printed 1 February 2008 (MN LATEX style file v1.4)

A Polarization Study of Radio Galaxies and Quasars selected from the Molonglo Complete Sample

C.H. Ishwara-Chandra[1,2], D.J. Saikia[1], V.K. Kapahi[1] and P. J. McCarthy[3]

[1] *National Centre for Radio Astrophysics, TIFR, Post Bag 3, Ganeshkhind, Pune 411 007, India*

[2] *Joint Astronomy Program, Department of Physics, Indian Institute of Science, Bangalore, 560 012, India*

[3] *The Observatories of the Carnegie Institution of Washington, 813 Santa Barbara st., Pasadena, CA 91101, USA*

ABSTRACT

We present total-intensity and linear-polarization observations made with the Very Large Array at λ20 and 6 cm of a representative sample of 42 radio galaxies and quasars selected from the Molonglo Complete Sample. The sources have been chosen to be of large size to probe the depolarizing medium on these scales using our present data and later with observations at lower frequencies with the Giant Metrewave Radio Telescope. The λ20 and 6 cm data are of similar resolutions and show that depolarization between these two wavelengths is seen largely in only those lobes which are within about 300 kpc of the parent galaxy. Examination of the depolarization of the lobes with arm-length asymmetry shows that depolarization is observed predominantly for the lobe which is closer to the nucleus. There is also a trend for the lobe closer to the nucleus to be brighter, consistent with the scenario that the nearer lobe is interacting with a denser environment which is responsible for the higher depolarization and greater dissipation of energy. We have also examined the depolarization asymmetry of the lobes on opposite sides of the nucleus for galaxies and quasars. This shows that the depolarization asymmetry for quasars is marginally higher than that for galaxies. The depolarization properties of our sample are possibly determined by an asymmetric environment as well as the effects of orientation.

Key words: galaxies: active - galaxies: nuclei - galaxies: jets - quasars: general - radio continuum: galaxies - polarization

1 INTRODUCTION

The discovery by Laing (1988) and Garrington et al. (1988) that double radio sources depolarize less rapidly on the side with the radio jet than on the opposite side provides the strongest evidence that the observed jet is on the approaching side, and its apparent asymmetry is due to relativistic beaming. The approaching side is seen through less of the depolarizing medium, and the Laing-Garrington effect can be understood as an orientation effect (cf. Garrington, Conway & Leahy 1991; hereinafter referred to as GCL91; Garrington & Conway 1991). In addition, Liu & Pooley (1991) found the more depolarized side of the source to have a steeper radio spectrum. A detailed study of a sample of quasars by Dennett-Thorpe et al. (1997) shows that the spectrum of the high-brightness features is indeed flatter on the jet side, while the low-brightness features have a flatter spectrum on the side with the longer lobe. They suggest that this is due to relativistic bulk motion in the high brightness features and differential synchrotron ageing in the extended emission.

The correlation of depolarization asymmetry with jet sidedness is also relevant for testing the unified scheme in which quasars and BL Lac objects are believed to be inclined at small angles to the line-of-sight while radio galaxies lie close to the plane of the sky (Barthel 1989; Antonucci 1993; Urry & Padovani 1995). In this scheme, the radio galaxies should exhibit a similar correlation of depolarization asymmetry with jet sidedness but of a smaller magnitude since the galaxies are inclined at large angles to the line of sight and the differential path length between the two lobes is smaller (cf. Holmes 1991; Saikia, Garrington & Holmes 1997). In addition to the effects of orientation, the depolarization of the lobes will also be affected by any asymmetry in the distribution of gas in the vicinity of the radio source. The possibility of an intrinsic asymmetry in the distribution of gas was suspected from the fact that the lobe on the jet side, which is approaching us, is often closer to the nucleus (Saikia 1981). An intrinsic asymmetry was demonstrated clearly by McCarthy, van Breugel & Kapahi (1991) who showed that there was invariably more emission-line gas on the side of the source which is closer to the nucleus. For a sample of 12 radio galaxies observed with the Very Large

Array (VLA), Pedelty et al. (1989) found the arm-length ratios to be correlated with the amount of depolarization and emission line gas. For the radio galaxies which are at large angles to the line-of-sight, it appears that the correlation of depolarization with arm-length asymmetry is stronger than with jet asymmetry, while the reverse is true for quasars (cf. Laing 1993).

In this paper we have studied the depolarization properties of a matched sample of radio galaxies and quasars selected from the Molonglo Reference Catalogue, to examine the effects of their environment as well as orientation on structural and depolarization asymmetries of these objects. Our objects were chosen to be of large angular and linear size to probe the depolarizing medium on these scales using high-frequency observations with the VLA and lower-frequency observations with the Giant Metrewave Radio Telescope (GMRT) in the future. We have also started a programme to make optical narrow-band images to study the emission-line gas as well as broad-band continuum images to study the environments of these objects. In this paper we present our total-intensity and linear polarization observations with the VLA BnA and CnB arrays at the L- and C-bands respectively. In Section 2 we describe the sample of sources, while the observations and observational results are presented in Sections 3 and 4 respectively. We then present our estimates of the depolarization of the lobes and hotspots, discuss their relationship with linear size and arm-length asymmetry, and any difference in depolarization asymmetry between radio galaxies and quasars. A study of the RM distributions in these sources and any relationship with line-emitting gas will be presented in a later paper.

2 THE SAMPLE OF SOURCES

Our sample has been selected from a complete sample of sources, the MRC/1Jy sample (McCarthy et al. 1996; Kapahi et al. 1998a, 1998b) which is a subset of the Molonglo Reference Catalogue (Large et al. 1981). The MRC/1 Jy sample consists of 558 sources which satsify the following criteria: $S_{408} \geq 0.95$ Jy; lie in the declination range $-30^\circ < \delta < -20^\circ$ and the right asension ranges $20^h\ 20^m$ to $06^h\ 15^m$ and $09^h\ 25^m$ to $14^h\ 03^m$ in B1950 co-ordinates; and lie outside the Galactic plane ($|b| > 20^\circ$). We have chosen FR II (Fanaroff & Riley 1974) sources from this sample with an angular size larger than about an arcminute to probe the depolarizing medium on these scales using the VLA and GMRT. We have chosen all quasars with a measured redshift greater than about 0.3, and a matched sample of galaxies of similar luminosity and redshift. The final sample of sources consists of 27 radio galaxies and 15 quasars, which are listed in Table 1. The redshifts for 0137−263, 0551−226, 0937−250, 0955−283, 1107−218, 1107−227, 1224−208 and 2042−293 have been estimated from their K magnitudes and are listed to only the first decimal place. The flux density at 1365 MHz and the spectral index between 1365 and 4935 MHz used for calculating the luminosity have been estimated from our observations. The luminosity, P, is in units of $\mathrm{WHz^{-1}sr^{-1}}$ and log $\mathrm{P_{1365}}$ is listed in the Table. The largest angular size (LAS) is expressed in arcsec and the corresponding largest linear size (LLS) is in kpc. The LAS has been estimated from the 1365 MHz images and represents the separation between the high brightness peaks in the outermost regions of emission on opposite sides of the nucleus. The radio galaxies and quasars in our sample have similar distributions of redshift, luminosity and linear size. For the galaxies, the median values of redshift and luminosity are 0.64 and 26.02 $\mathrm{WHz^{-1}sr^{-1}}$, compared to 0.71 and 26.00 $\mathrm{WHz^{-1}sr^{-1}}$ for the quasars. The corresponding values of angular and linear sizes are $72''$ and 595 kpc for the galaxies and 75 $''$ and 597 kpc for the quasars. We have assumed an Einstein de-Sitter Universe with $\mathrm{H_\circ} = 50$ km $\mathrm{s^{-1}}$ $\mathrm{Mpc^{-1}}$.

Table 1. The sample of sources

Source Name	Id	z	$\mathrm{S_{1365}}$ mJy	$\mathrm{P_{1365}}$ W/Hz/sr	LAS $''$	LLS kpc
0017-207	Q	0.545	467	25.76	98	722
0058-229	Q	0.706	396	25.95	63	505
0133-266	Q	1.53	348	26.61	53	455
0137-263	G	1.1	509	26.51	79	679
0148-297	G	0.41	2778	26.28	148	961
0325-260	G	0.638	286	25.70	58	447
0346-297	G	0.413	620	25.65	142	929
0428-281	G	0.65	956	26.25	79	617
0437-244	Q	0.84	459	26.19	128	1059
0454-220	Q	0.533	1993	26.35	94	683
0551-226	G	0.8	330	26.00	53	438
0937-250	G	0.9	445	26.28	72	607
0938-205	G	0.371	444	25.39	72	445
0947-249	G	0.854	1487	26.75	71	595
0955-283	G	0.8	470	26.14	96	791
1022-250	G	0.34	338	25.20	61	363
1023-226	G	0.586	298	25.64	66	495
1025-229	Q	0.309	489	25.28	198	1105
1026-202	G	0.566	664	25.95	61	456
1029-233	G	0.611	403	25.80	80	609
1052-272	Q	1.103	553	26.56	89	760
1107-218	G	1.5	302	26.53	62	531
1107-227	G	2.0	781	27.40	72	590
1126-290	G	0.41	1086	25.89	111	725
1224-208	G	1.5	268	26.57	61	519
1226-297	Q	0.749	435	26.00	74	597
1232-249	Q	0.352	1988	25.97	110	660
1247-290	Q	0.77	696	26.27	60	489
1257-230	Q	1.109	788	26.65	53	458
1358-214	G	0.5	317	25.34	96	681
2035-203	Q	0.516	752	25.87	71	514
2040-236	Q	0.704	428	25.89	64	510
2042-293	G	1.9	414	26.99	79	655
2045-245	G	0.73	639	26.21	76	611
2118-266	G	0.343	403	25.24	89	526
2132-235	G	0.81	333	26.02	58	482
2137-279	G	0.64	455	25.93	57	442
2213-283	Q	0.946	820	26.53	75	633
2311-222	G	0.434	965	25.85	92	616
2325-213	G	0.58	986	26.17	84	632
2338-290	Q	0.446	427	25.51	79	532
2348-235	G	0.952	503	26.34	67	570

Table 2. Observing schedule

Array Conf.	Freq. of obs. MHz	Band-width MHz	Date	Total time hr
BnA	1365	50	1995 Sept. 20	16.0
	1665	25		
CnB	4635	50	1996 Jan. 20,31	10.5
	4935	50		

3 OBSERVATIONS AND ANALYSES

The observations were made with scaled arrays of the Very Large Array of National radio Astronomy Observatory (Thompson 1980) in order to get similar resolutions at the L- and C-bands. A summary of the observations is presented in Table 2. Short scans of unresolved sources selected from the VLA Calibrator Manual (Perley 1996) were interspersed for phase calibraton. At both the bands two widely separated IFs with bandwidths of 50 MHz were used except for the one centered at 1665 MHz where the bandwidth was only 25 MHz. The IFs were separated by about 300 MHz so that the rotation measure (RM) could be determined reliably. One source, 1358−214, was not observed at the C band due to technical problems. Most sources were observed in two scans at different hour angles, each lasting about 10 min.

The data for each IF at both bands were edited and calibrated separately using the NRAO `AIPS` package. All flux densities are on the Baars et al. (1977) scale, with 3C48 and 3C286 being the primary flux density calibrators. To determine the absolute position angle both 3C138 and 3C286 were observed while the instrumental polarization was determined by observing the unresolved calibtrators, over a range of parallactic angles. We have corrected for ionospheric Faraday rotation, which could be significant at the L-band, using the routines in the `AIPS` package (cf. Chiu 1975). Comparing the polarization position angles of 3C286 and 3C138 before and after applying the ionospheric Faraday correction based on this model, we find the difference in PA to be within about 5°. After completing the continuum and polarization calibration, images of the sources were made with uniform weighting to all baselines using the `AIPS` task `MX` and `IMAGR`. Several iterations of self calibrations were also done to correct for residual phase errors. The final data set was used to make images in the Stokes parameters I, Q and U. A given source has been restored with a beam of the same size at both the L and C bands. We have also made circular polarization or Stokes V images of all sources to estimate the rms noise in our maps. The ratio of the peak intensity to the rms noise in the total-intensity images is typically more than about 1000:1 at the L band.

The maps of polarized intensity, $p = (Q^2 + U^2)^{1/2}$, and position angle, $\chi = 0.5\tan^{-1}(U/Q)$ were made by combining the Q and U maps. The resulting polarized intensity image has a positive bias which has been corrected using the `AIPS` task `POLCO`, and also all pixels of amplitude $\leq 2\sigma$ were blanked, where σ is the noise in the Q or U maps. The polarized flux density was estimated from this image, while the rms noise on the polarized intensity map has been estimated before applying the bias correction. The images of the sources at one IF in each of the two bands are presented in Figure 1, with the fractional polarization vectors superimposed on the total-intensity contours. The image of the source, 1358−214, for which we have data at only the L-band is shown at the end of Figure 1. The size of the restoring beam and the rms noise in the total-intensity and polarization images for these frequencies are listed in Table 3. The corresponding values for the other frequency in each band are similar.

Table 3. Image parameters

Source Name	beam maj	beam min	beam PA	22 cm σ_I	22 cm σ_p	6.08 cm σ_I	6.08 cm σ_p
	″	″	°	μJy/beam			
0017−207	4.5	3.5	+70	180	60	55	55
0058−229	4.2	3.5	+80	107	65	44	50
0133−266	5.0	3.0	+60	86	60	43	65
0137−263	5.0	3.0	+60	149	60	55	55
0148−297	4.5	3.5	+60	246	70	211	50
0325−260	4.2	4.2	00	119	65	40	50
0346−297	4.2	4.2	00	141	60	55	50
0428−281	4.5	3.5	−70	146	65	50	65
0437−244	4.5	3.2	−70	96	65	50	55
0454−220	4.5	3.0	−70	194	60	75	60
0551−226	6.0	3.5	−50	111	60	50	50
0937−250	8.0	4.5	−50	142	61	55	55
0938−205	7.5	5.0	−50	122	58	54	60
0947−249	8.0	4.0	−50	178	65	109	50
0955−283	6.0	6.0	00	180	66	65	55
1022−250	6.0	6.0	00	238	60	67	65
1023−226	8.0	4.5	−50	148	58	47	50
1025−229	8.0	4.5	−50	167	62	70	50
1026−202	8.0	4.2	−50	161	60	56	65
1029−233	6.0	4.5	−50	204	58	72	55
1052−272	6.0	5.0	−50	150	60	50	60
1107−218	6.5	4.5	−50	125	60	50	55
1107−227	6.5	4.5	−50	234	65	60	60
1126−290	6.0	5.0	−50	201	60	81	55
1224−208	7.0	4.2	−50	192	60	75	60
1226−297	7.0	4.5	−50	361	61	82	55
1232−249	7.0	4.5	−50	1352	85	87	55
1247−290	7.0	5.5	−50	250	60	75	60
1257−230	7.0	4.5	−50	545	70	53	50
1358−214	6.5	3.0	−50	178	60	–	–
2035−203	7.0	3.0	+50	238	60	79	65
2040−236	6.4	3.0	+50	194	65	59	50
2042−293	8.4	3.0	+40	192	65	65	60
2045−245	7.5	3.0	+50	155	60	53	65
2118−266	7.5	3.0	+50	244	60	72	55
2132−236	7.5	3.0	+50	100	70	51	60
2137−279	7.5	3.0	+50	197	60	51	60
2213−283	6.5	3.0	+50	166	65	55	55
2311−222	5.0	3.0	+60	201	60	62	65
2325−213	5.0	3.0	+60	159	148	55	50
2338−290	5.0	3.5	+50	261	60	76	55
2348−235	5.0	3.0	+60	113	136	76	60

3.1 Observational results

We have estimated the total intensity and polarized flux density of each lobe of a source by specifying a rectangular box such that all the regions of the lobe with total flux density more than about 5 times the rms noise per beam in the total-intensity image are included in the box. Following Garrington et al. (1991), we have set the box based on the 20 cm image and a box of the same size has been used for the λ6 cm image. These values were used to estimate the degree of polarization and depolarization between these two wavelengths for the lobes. In addition, we have also estimated the degree of polarization and depolarization for the hotspots by specifying a small box of 5×5 arcsec^2 centred on the pixel of maximum brightness in each lobe as seen on the λ20 cm image. In our images the pixel size is one arcsec at both bands. The integrated and peak values are listed in Table 4 which is arranged as follows. Column 1: source name; column 2: component designation where N, S, W and E denote north, south, west and east respectively; columns 3 and 4: the total intensity, S_I, and the degree of scalar polarization, m_l=($\Sigma p/\Sigma I$) × 100 %, for the entire component at λ22 cm; columns 5 and 6: the peak brightness of the lobe, S_p, and the degree of polarization of the hotspot, m_{hs}, at λ22 cm; columns 7 to 10: same as columns 3 to 6, but at λ18 cm; columns 11 to 14: same as columns 3 to 6, but at λ6.47 cm; columns 15 to 18: same as columns 3 to 6, but at λ6.08 cm.

3.2 Error estimates

For our interpretation we need to estimate the error in the degree of polarization and the depolarization ratio between the L and C bands. The measurement errors in the total- and polarized- flux density are estimated from the off-source rms fluctuations. In the region over which we measure the total flux density, this error is $N_I^{1/2}\delta_I$, and the error in polarization maps is $N_p^{1/2}\delta_p$, where N_I and N_p are the number of non-blank beam areas and δ_I and δ_p are the off-source rms fluctuations per beam in the total- and polarized-intensity maps. The fractional polarization m and the fractional error in m are $m = \frac{\Sigma p}{\Sigma I}\times 100\%$ and $\delta m = (\frac{\sigma_p}{\Sigma p}+\frac{\sigma_I}{\Sigma I})m$ respectively. From the internal consistency of the data, we have estimated the uncertainity in polarization calibration to be better than about 0.3%. Combining this with the fractional error in m, the resultant uncertainity in m is $\sigma_m = [(\delta m)^2 + 0.3^2]^{1/2}$%.

The depolarization DP and the error in DP are as follows: DP= m_{20}/m_6 ; σ_{DP} = DP × $[(\frac{\sigma_{m20}}{m_{20}})^2 + (\frac{\sigma_{m6}}{m_6})^2]^{1/2}$, since the errors on m_{20} and m_6 are uncorrelated. The errors in our estimates of fractional polarization are in the range 0.3% - 0.6%, while the estimated errors in DP are less than about 0.08 in most cases.

4 RESULTS AND DISCUSSION

In our sample of 41 sources with information at both bands, there are a total of 82 lobes. However, 6 of these lobes, namely 0346−297N, 0938−205N, 1025−229S, 1226−297N, 2040−236W and 2118−266W, have been excluded from the analysis becasue they are very weak and diffuse and their polarization information could not be determined reliably. The derived parametes for the remaining 76 lobes are presented in Table 5 which is arranged as follows. Column 1: source name and letter designation identifying the component; column 2: the linear separation in kpc of the peak of the lobe, including the hotspot at the angular resolution of the image, from the radio core or the optical position, if a core has not been detected; column 3: the ratio of separation of the component from the core/optical position to that of the component on the opposite side; columns 4 and 5: the depolarization DP=m_{20}/m_6 and the error in DP for the entire lobe including the hotspot; columns 6 and 7: the depolarization and the error in DP for the hotspots.

The distributions of the degree of polarization of the lobes, m_l, at λ6 cm range from about 2.4 to 18.2%, with a median value of about 10%. This is similar to the sample of sources observed by GCL91, where the median value on the jet as well as counter-jet side is 10.7%. We have also examined the distributions for the sample of 40 strong lobes defined to be those with $S_{peak} \geq$25 mJy at λ6 cm, and find their polarization to be similar to those of the weaker sources. The degree of polarization for the hotspots in the samples of strong and weak lobes are also similar. At λ20 cm, the distribution of the degree of polarization, m_{20}, ranges from 2.8 to 18.4%, with a median value of again about 10%. The median values for the strong and weak source samples are about 9.3 and 11.0 respectively. The weak sources have higher errors and the difference is margnial. There is a similar difference for the hotspot values. The degree of polarization in our lobes is only marginally higher than the jet sides at λ20 cm of the GCL91 sample where the median value is 8%, although the counter-jet sides in GCL91 exhibit significant depolarization. The values of the depolarization parameter, DP = m_{20}/m_6, for the lobes range from about 0.54 to 2.95, with median values of about 1 for the strong lobes, and about 1.1 for the weaker ones. The values of DP for the hotspots are similar.

GCL91 suggested that X-ray emitting gas associated with poor clusters of galaxies could produce the observed depolarization in their sample. Assuming similar parameters as those used by GCL91 for the depolarizing gas in an unresolved foreground Faraday screen (Burn 1966), and using the median values of size and redshift for our sources, we expect the depolarization between λ20 and λ6 cm in the observed frame to be close to about 1 for galaxies and about 0.8 for quasars. However, there are significant uncertainties in the assumed parameters of GCL91, and the Faraday screens may also have partially resolved structures. We hope to place better constraints on these values after making observations over a longer wavelength range. Significantly stronger depolarization will be seen at longer wavelengths, say between λ20 cm and either λ49 cm or λ90 cm. Since long-wavelength measurements are still being planned using the GMRT, we discuss in this paper any possible dependence of depolarization on linear size and lobe separation ratio using the present data. We also discuss the depolarization asymmetry of the oppositely directed lobes for both radio galaxies and quasars and comment on whether this is consistent with the unified scheme. In the following sections, we first present the data for the entire sample and then focus on the strong-lobe sample where the errors are smaller and the effect of poor signal to noise ratio will be minimum.

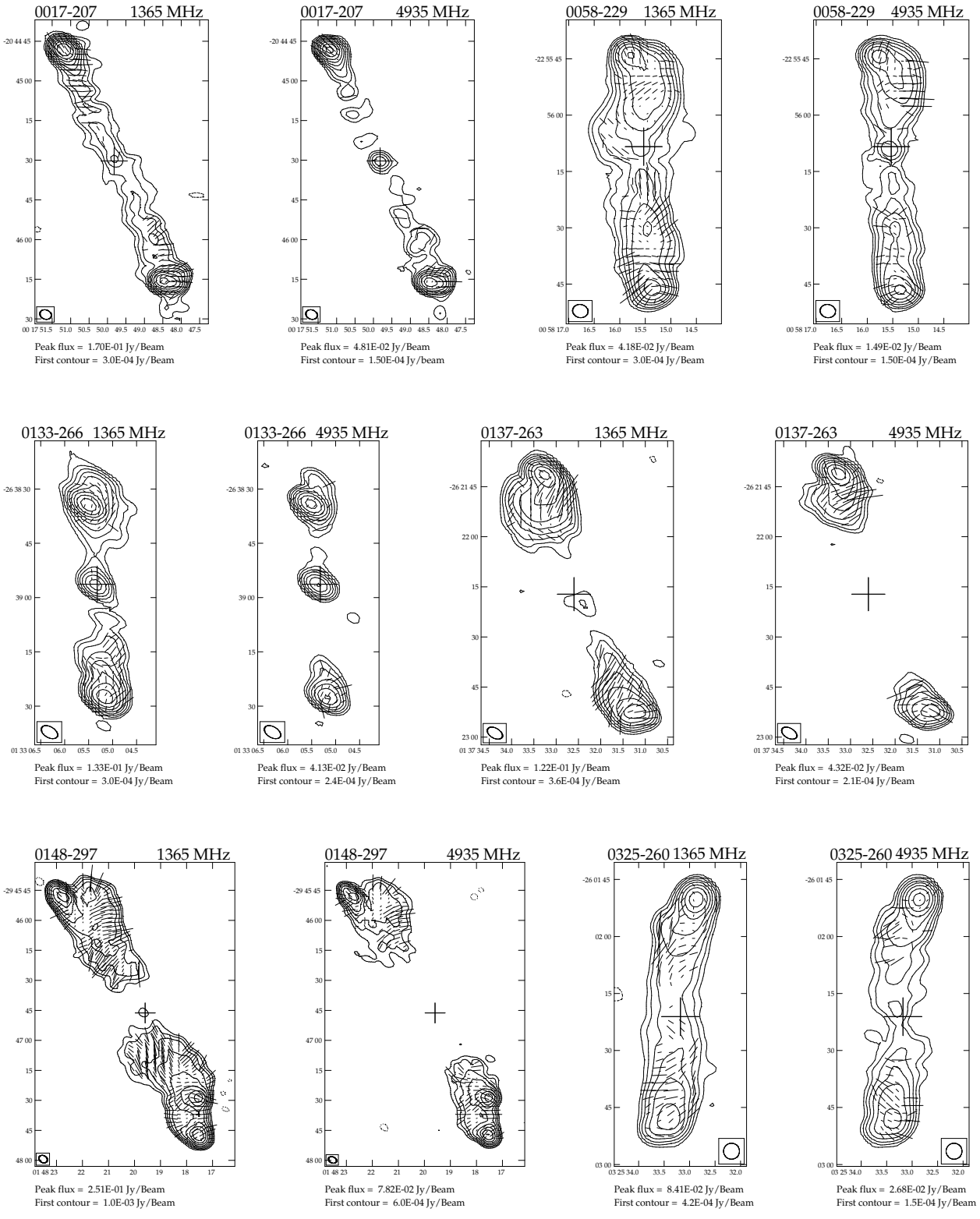

Figure 1. Images of the sample of sources at 1365 and 4935 MHz. The image for 1358−214, for which there is data at only the L-band is shown at the end of this figure. The polarization vectors are superimposed on the total-intensity contours. The restoring beam is shown by the ellipse enclosed within a box, while the cross indicates the position of the optical object. The contour levels are -2, -1, 1, 2, 4, 8, 16, 32, 64, 128, 256, 512 times the base level given below each figure. One arc second length of polarization vector corresponds to 5% polarization. X axis is right ascension and Y axis is declination in B1950 co ordinates.

Remaining part of figure 1 is available via anonymous ftp from

ftp://ncra.tifr.res.in/pub/ishwar/

or from MNRAS Vol 300, page 269.

In case of problems, please contact

ishwar@ncra.tifr.res.in

Table 4. Flux density and degree of polarization at different wavelengths

Source		22 cm				18 cm				6.47 cm				6.08 cm			
Name	Cp	S_I	m_l	S_p	m_h	S_I	m_l	S_p	m_h	S_I	m_l	S_p	m_h	S_I	m_l	S_p	m_h
0017−207	N	260	13.8	170	15.6	191	14.3	140	16.1	75	13.4	51	16.0	70	14.1	48	17.2
	S	202	9.4	99	8.6	173	8.9	85	8.3	62	9.7	33	6.6	58	7.6	32	6.7
0058−229	N	225	5.8	42	10.3	173	7.6	34	13.1	64	8.9	17	12.5	57	8.5	15	12.2
	S	158	11.0	30	14.3	125	9.3	25	12.6	49	9.5	13	11.1	44	8.5	12	10.4
0133−266	N	196	4.2	133	4.2	155	4.2	110	4.2	58	3.0	44	3.2	53	4.5	41	3.7
	S	134	8.3	67	6.4	102	7.4	54	6.8	30	6.9	18	6.3	26	7.7	17	7.5
0137−263	N	384	12.5	122	8.3	307	12.0	105	8.3	102	12.6	45	11.0	93	13.5	43	11.2
	S	125	16.6	37	17.6	99	16.4	30	18.3	31	16.9	12	14.8	28	15.3	11	18.9
0148−297	N	1150	17.3	197	24.2	862	18.7	168	26.0	334	15.0	74	24.0	311	16.6	65	27.0
	S	1628	18.3	251	21.3	1289	19.3	217	22.7	460	16.3	92	19.8	436	17.6	78	23.2
0325−260	N	168	6.3	84	3.7	140	5.6	70	3.2	53	4.0	29	2.1	48	3.9	27	2.0
	S	117	9.9	24	9.8	93	9.6	19	10.8	35	10.0	8.1	7.8	30	8.2	7.1	8.2
0346−297	N	71	21.0	3.9	33.0	45	22.9	2.8	37.7	20	–	1.2	–	14	–	0.97	–
	S	549	18.4	55	17.1	424	17.7	43	16.6	142	15.3	18	13.5	128	16.1	16	14.5
0428−281	E	424	9.4	229	4.9	326	9.0	189	5.0	114	6.9	70	4.4	106	7.5	66	4.6
	W	532	10.0	318	7.3	426	9.8	271	7.4	154	8.6	105	7.2	142	10.4	98	7.9
0437−244	N	280	8.0	66	12.9	197	7.8	53	12.0	73	8.2	22	13.0	66	7.8	20	13.0
	S	160	12.2	44	6.8	108	9.2	36	7.0	41	10.3	15	5.7	37	6.7	14	4.2
0454−220	N	716	6.9	199	7.6	553	8.6	163	9.0	226	10.5	65	9.0	212	10.6	60	9.6
	S	1006	10.5	380	10.9	792	10.5	312	11.4	283	10.9	107	11.7	264	10.7	99	11.8
0551−226	N	151	9.6	25	14.1	87	12.7	17	15.9	46	9.2	8.8	14.8	40	11.8	8.0	14.5
	S	179	8.7	29	14.6	104	10.7	19	18.0	45	9.6	9.1	17.0	43	9.9	8.3	18.1
0937−250	N	175	8.8	56	9.1	129	11.0	46	9.3	31	7.4	17	4.1	30	10.7	17	5.4
	S	270	5.8	100	5.8	215	5.0	81	4.7	70	5.2	29	4.3	64	5.4	27	5.2
0938−205	N	224	2.3	23	7.2	170	2.9	19	7.6	68	–	8.7	–	60	–	8	–
	S	220	11.9	40	9.8	167	12.0	32	9.1	66	7.0	16	5.7	59	11.2	16	8.1
0947−249	N	1087	10.4	602	13.1	845	12.3	487	13.4	243	15.1	159	13.0	227	16.2	149	14.0
	S	336	6.6	223	6.1	267	6.4	180	5.7	89	6.4	64	5.7	83	6.5	60	5.8
0955−283	E	171	13.9	53	14.7	122	13.5	43	16.6	44	15.2	17	18.0	40	14.0	17	16.6
	W	299	8.7	192	9.5	236	8.7	158	9.7	92	8.3	60	9.2	86	8.6	56	9.4
1022−250	E	127	5.6	37	8.7	87	5.1	28	8.2	33	4.5	12	8.6	29	6.4	11	7.2
	W	212	12.6	52	17.2	160	12.7	41	17.1	62	12.4	19	13.8	57	12.2	18	13.1
1023−226	N	197	5.2	83	6.9	156	4.7	68	6.2	64	3.7	30	4.4	60	4.1	29	5.7
	S	75	2.8	46	2.9	60	2.8	37	3.6	25	2.4	16	2.5	22	2.5	15	3.1
1025−229	N	250	9.0	78	5.8	181	8.8	67	5.9	59	7.1	27	5.8	52	8.5	24	5.9
	S	176	10.7	20	9.4	122	10.5	17	12.4	38	–	6.6	–	33	–	6.2	–
1026−202	N	262	11.4	69	9.8	215	11.1	57	9.5	81	9.3	24	10.8	75	9.6	22	11.1
	S	401	6.8	134	8.3	321	7.8	110	9.8	117	8.0	45	7.9	111	7.7	43	7.9
1029−233	E	290	14.2	116	11.4	220	15.1	94	12.7	91	14.4	40	13.9	87	14.3	38	14.3
	W	86	11.0	38	9.4	66	10.3	30	9.9	28	9.9	13	9.2	25	10.7	12	10.8
1052−272	N	345	6.2	192	5.7	263	7.1	153	6.4	74	8.7	49	8.1	70	8.4	46	8.0
	S	205	7.9	69	10.7	164	7.6	56	9.6	54	7.8	20	8.6	51	6.7	20	8.1
1107−218	E	105	5.1	56	4.1	83	6.9	48	5.0	33	5.3	21	4.2	30	5.8	20	4.2
	W	197	7.2	124	10.5	153	7.8	103	11.3	60	8.0	43	10.7	55	10.0	40	12.0
1107−227	N	520	8.0	346	5.1	398	7.5	271	5.4	104	7.4	81	8.4	96	7.7	75	9.1
	S	261	12.6	153	15.7	195	11.6	114	15.1	47	9.2	30	8.7	41	9.6	24	8.1
1126−290	N	352	11.6	73	6.5	275	11.3	60	6.8	71	14.4	24	5.8	65	13.7	23	5.8
	S	734	12.1	169	13.1	565	11.9	146	13.6	193	12.4	64	13.4	176	12.2	62	13.2
1224−208	N	188	15.4	71	19.5	141	18.1	54	20.6	42	19.5	20	16.9	38	18.2	18	18.1
	S	80	10.0	34	10.6	56	11.4	25	10.9	20	5.6	9.6	9.2	18	8.1	9.2	9.3
1226−297	N	17	–	12	–	12	–	10	–	6.8	–	5.3	–	6.8	–	5.3	–
	S	416	12.8	366	14.4	345	13.2	308	14.8	147	13.7	132	15.6	138	14.2	124	16.1

Source		22 cm				18 cm				6.47 cm				6.08 cm			
Name	Cp	S_I	m_l	S_p	m_h	S_I	m_l	S_p	m_h	S_I	m_l	S_p	m_h	S_I	m_l	S_p	m_h
1232−249	N	1084	9.6	457	13.0	901	10.1	397	12.8	365	9.4	163	11.7	343	8.9	154	11.6
	S	878	8.3	405	5.4	722	8.0	357	5.2	297	6.6	169	4.5	280	7.2	158	5.4
1247−290	N	416	11.9	290	12.3	335	13.1	234	13.4	121	12.7	88	13.2	115	11.9	80	12.9
	S	253	11.9	133	8.6	205	11.5	110	8.7	75	5.9	46	4.7	69	8.3	42	6.8
1257−230	N	259	5.2	213	4.1	175	5.8	151	4.4	63	3.8	49	3.7	57	4.3	44	3.9
	S	514	5.0	456	5.1	398	5.3	373	5.2	167	3.6	147	4.1	158	3.8	139	4.5
1358−214	N	211	15.9	58	5.1	163	16.4	45	6.3	–	–	–	–	–	–	–	–
	S	172	13.7	39	11.3	155	11.6	33.6	12.2	–	–	–	–	–	–	–	–
2035−203	E	563	13.8	417	13.1	487	13.5	363	13.8	225	13.6	175	14.7	213	14.8	167	15.5
	W	154	17.4	21	18.1	126	15.5	17	15.9	43	15.7	7.2	16.6	39	10.8	6.7	14.4
2040−246	E	247	9.1	105	14.2	203	9.1	86	15.2	82	8.8	37	14.4	76	9.4	35	15.5
	W	50	6.5	15	6.2	38	4.3	12	5.6	13	–	4.9	–	12	–	4.2	–
2042−293	N	286	9.6	48	9.1	209	10.4	39	8.7	71	4.8	16	6.6	65	6.3	15	6.6
	S	128	12.8	23	13.7	88	14.0	17	14.5	32	10.7	7.4	15.4	26	12.2	6.8	12.5
2045−245	N	383	7.4	180	7.8	303	8.5	146	9.3	96	9.6	52	11.9	88	10.3	48	12.9
	S	256	15.1	70	17.7	199	14.2	56	18.0	70	11.79	20	14.5	62	13.0	18	15.9
2118−266	E	277	7.8	78	4.1	212	7.2	65	4.5	84	5.0	28	4.4	77	4.9	26	3.5
	W	81	8.5	5	12.0	48	9.7	3.8	13.7	16	–	1.2	–	18	–	1.5	–
2132−236	N	157	10.8	72	9.1	121	11.2	60	9.5	44	11.2	24	9.9	39	9.7	23	10.0
	S	177	7.6	122	7.6	136	8.6	100	8.1	48	8.1	36	8.4	43	7.3	33	7.8
2137−279	N	170	8.1	46	10.5	132	8.1	37	9.9	46	6.4	14	9.5	42	6.1	13	8.5
	S	285	11.4	168	12.6	215	13.5	135	13.8	71	13.1	45	13.8	67	14.3	42	14.4
2213−283	E	432	14.0	126	21.9	347	13.3	103	21.7	115	12.2	35	20.1	107	11.7	32	19.4
	W	328	5.2	166	5.5	253	5.6	131	5.5	73	9.6	41	9.0	67	9.7	37	8.8
2311−222	E	816	11.8	577	9.6	666	12.0	505	9.9	278	11.4	205	10.7	262	11.2	194	10.8
	W	144	7.0	64	4.0	113	5.8	53	3.9	46	3.8	23	3.1	44	2.4	22	2.9
2325−213	N	378	13.7	113	9.9	291	13.5	91	10.7	107	11.3	34	9.5	99	11.3	32	9.5
	S	608	9.1	136	14.2	461	9.7	109	14.7	159	9.6	63	14.5	146	9.0	40	14.6
2338−290	N	166	11.5	58	15.4	128	11.0	47	15.5	56	8.9	21	13.9	49	10.2	21	14.4
	S	216	15.0	17	16.3	146	15.6	14	15.2	59	13.8	5.8	15.0	51	12.7	5.2	17.0
2348−290	N	199	13.5	55	13.6	157	13.2	45	12.9	57	10.0	19	8.8	51	9.7	18	8.6
	S	299	13.9	69	14.0	235	16.3	57	14.7	83	16.9	22	12.5	77	16.4	21	12.7

4.1 Linear separation of the lobe and depolarization

We present the plot of the linear separation of each lobe from the core or optical position against the depolarization parameter, DP=m_{20}/m_6, of the entire lobe in Figure 2, and against the corresponding DP values of the hotspots in Figure 3. The upper panel in each figure shows the plot for the entire data while the bottom one shows only for the sample of strong lobes which have been defined to have S_{peak}(6 cm) > 25 mJy. These figures show that evidence of depolarization is seen more frequently in the sources of smaller linear size. Considering the entire sample, 20 of the 43 lobes with a linear separation L < 300 kpc have DP < 1, while for those with L > 300 kpc, only 7 of 33 have DP < 1. A Kolmogorov-Smirnov test shows that the DP distributions for lobes with L < 300 and > 300 kpc are different at a significance level of about 99 per cent. A similar but weaker trend is seen for the hotspots. Concentrating only on those which show significant depolarization, say DP< 0.9, there are 17 lobes, 15 of which have L< 300 kpc, and 15 hotspots, 11 of which have L< 300 kpc.

These trends for the sample of strong lobes are seen clearly in the Figures. Above a linear separation, L, of 300 kpc, there is little evidence of depolarization, while lobes and hotspots below this value often have DP significantly less than 1. Here 13 of the 24 lobes with L< 300 kpc have DP < 1.0, while this is true for only 5 of 16 with L>300 kpc. All the 8 lobes with DP < 0.9 have L< 300 kpc. A similar trend is also seen while considering the values for the hotspots where 10 of 24 with L<300 kpc have DP< 0.9 while this is true for only 2 of the 16 lobes with L>300 kpc.

GCL91 reported that the depolarization parameter on the counter-jet side, DP_{cj}, decreases with increasing distance from the core, while for the jet side, DP_j, no such trend is seen. For a sample of 12 galaxies, observed by Pedelty et al. (1989) with the VLA at λ20 and 6 cm, DP is about 0.3 for the smaller sources with linear separations L within about 100 kpc, and increases to about 1 for a separation of about 300 kpc which is amongst their largest objects. Our source sizes are about a factor of two larger than those of Pedelty et al. The smallest separation in our sample of strong lobes is about 150 kpc and has a DP of about 0.54 ± 0.04. For L > 300 kpc, almost all sources show no evidence of strong depolarization. However, a number of sources appear to have DP > 1. We have examined the data for both strong and weak sources, and also for sources observed on different days and find no reasonable cause for any systematic error. A similar trend for dependence of DP on L was also reported for relatively nearby radio galaxies by Jägers (1986) and Strom & Jägers (1988) from observations with the WSRT at λ20 and 49 cm. They find DP_{21}^{49} to be about 0.6 at L of about

Table 5. Derived parameters of the lobes and hotspots

Source Name	L kpc	r_θ	DP$_l$	σ_{DP_l}	DP$_h$	σ_{DP_h}
0017−207N	348	0.93	0.98	0.04	0.91	0.03
0017−207S	374	1.08	1.24	0.08	1.84	0.19
0058−229N	201	0.66	0.68	0.05	0.80	0.04
0058−229S	305	1.52	1.29	0.09	1.27	0.07
0133−266N	189	0.71	0.94	0.10	1.11	0.13
0133−266S	266	1.41	1.08	0.09	0.98	0.07
0137−263N	323	0.89	0.92	0.03	0.59	0.04
0137−263S	363	1.13	1.09	0.06	0.99	0.05
0148−297N	509	1.11	1.04	0.03	0.93	0.02
0148−297S	458	0.90	1.04	0.03	1.02	0.02
0325−260N	241	1.17	1.63	0.19	1.93	0.39
0325−260S	206	0.85	1.21	0.10	1.27	0.13
0346−297S	383	0.70	1.14	0.04	1.22	0.07
0428−281E	352	1.32	1.24	0.07	1.02	0.08
0428−281W	266	0.76	0.96	0.04	0.87	0.06
0437−244N	415	0.64	1.02	0.07	1.13	0.06
0437−244S	645	1.55	1.83	0.20	1.82	0.28
0454−220N	239	0.54	0.65	0.03	0.60	0.04
0454−220S	445	1.86	0.98	0.04	0.95	0.06
0551−226N	258	1.43	0.82	0.05	0.67	0.05
0551−226S	180	0.70	0.87	0.05	0.96	0.07
0937−250N	270	0.80	0.82	0.06	1.74	0.32
0937−250S	339	1.25	1.07	0.09	0.98	0.13
0938−205S	328	2.79	1.06	0.05	1.07	0.17
0947−249N	242	0.69	0.64	0.02	0.92	0.03
0947−249S	353	1.46	1.01	0.07	0.86	0.08
0955−283E	375	0.90	1.02	0.05	1.08	0.06
0955−283W	417	1.11	1.00	0.05	0.99	0.05
1022−250E	251	2.15	0.88	0.11	1.32	0.07
1022−250W	116	0.46	1.03	0.04	1.28	0.19
1023−226N	214	0.75	1.24	0.13	1.33	0.17
1023−226S	285	1.34	1.10	0.24	1.03	0.33
1025−229N	568	1.05	1.05	0.08	1.03	0.12
1026−202N	241	1.11	1.19	0.06	1.03	0.07
1026−202S	217	0.90	0.88	0.06	0.86	0.07
1029−233E	299	0.97	0.99	0.03	0.82	0.03
1029−233W	310	1.03	1.03	0.07	1.01	0.12
1052−272N	197	0.35	0.74	0.05	0.66	0.05
1052−272S	564	2.86	1.18	0.08	0.94	0.10
1107−218E	269	1.02	0.87	0.09	1.10	0.16
1107−218W	264	0.98	0.72	0.04	0.86	0.04
1107−227N	274	0.87	1.03	0.06	0.45	0.05
1107−227S	316	1.15	1.31	0.06	1.78	0.14
1126−290N	401	1.24	0.85	0.04	0.59	0.12
1126−290S	325	0.81	0.99	0.04	1.04	0.05
1224−208N	156	0.43	0.85	0.03	0.92	0.04
1224−208S	363	2.32	1.25	0.11	1.20	0.14
1226−297S	309	1.07	0.90	0.03	0.90	0.03
1232−249N	356	1.17	1.08	0.05	0.98	0.08
1232−249S	304	0.85	1.16	0.07	1.05	0.08
1247−290N	195	0.66	1.00	0.04	0.97	0.04
1247−290S	297	1.52	1.43	0.08	1.22	0.09
1257−230N	217	0.88	1.22	0.12	1.21	0.15
1257−230S	245	1.13	1.32	0.13	1.42	0.16
2035−203E	279	1.13	0.93	0.03	0.85	0.03
2035−203W	246	0.88	1.60	0.09	1.26	0.10
2040−236E	153	0.43	0.97	0.05	0.97	0.05
2042−293N	383	1.40	1.52	0.11	2.70	0.64
2042−293S	274	0.71	1.05	0.07	1.37	0.14
2045−245N	269	0.78	0.73	0.04	0.70	0.04
2045−245S	343	1.27	1.16	0.05	1.14	0.04
2118−266E	247	0.88	1.61	0.15	1.20	0.19
2132−236N	275	1.33	1.11	0.07	0.92	0.05
2132−236S	207	0.75	1.05	0.07	0.98	0.07
2137−279N	250	1.30	1.33	0.11	1.16	0.15
2137−279S	193	0.77	0.80	0.03	0.91	0.03
2213−283E	469	2.86	1.20	0.04	1.15	0.03
2213−283W	164	0.35	0.54	0.04	0.62	0.04
2311−222E	281	0.84	1.05	0.04	0.94	0.04
2311−222W	335	1.19	2.95	0.47	1.33	0.21
2325−213N	355	1.27	1.21	0.05	1.11	0.06
2325−213S	278	0.78	1.01	0.05	0.97	0.04
2338−290N	275	0.98	1.13	0.07	1.07	0.04
2338−290S	282	1.03	1.18	0.07	1.02	0.12
2348−235N	285	1.00	1.40	0.07	1.32	0.11
2348−235S	286	1.00	0.84	0.03	1.09	0.05

250 kpc, which is consistent with our DP$_6^{20}$ values at this separation.

Considering the galaxies and quasars separately, there is no striking difference in their depolarization values. This is partly because we have selected large sources. The observed depolarization is likely to be affected by intrinsic asymmetries in addition to any path-length differences between quasars and radio galaxies. We examine the depolarization asymmetry between the oppositely directed lobes for radio galaxies and quasars in Section 4.4.

4.2 Lobe separation ratio and depolarization

For a sample of 3CR radio galaxies, McCarthy, van Breugel & Kapahi (1991) showed that there is more emission-line gas on the side of the lobe which is closer to the nucleus, suggesting an environmental origin for the observed arm-length asymmetries rather than being due to light travel time across the source axes. For the sample of galaxies observed by Pedelty et al. (1989), the depolarization is almost always stronger for the lobe closer to the nucleus. In 5 of their 8 sources that have extended emission-line gas, there is a spatial correlation between depolarization and emission-line gas, while for the remaining three, the gas is more centrally located and the sources are not strongly depolarized. Our sample of sources has not been chosen on the basis of

[t]

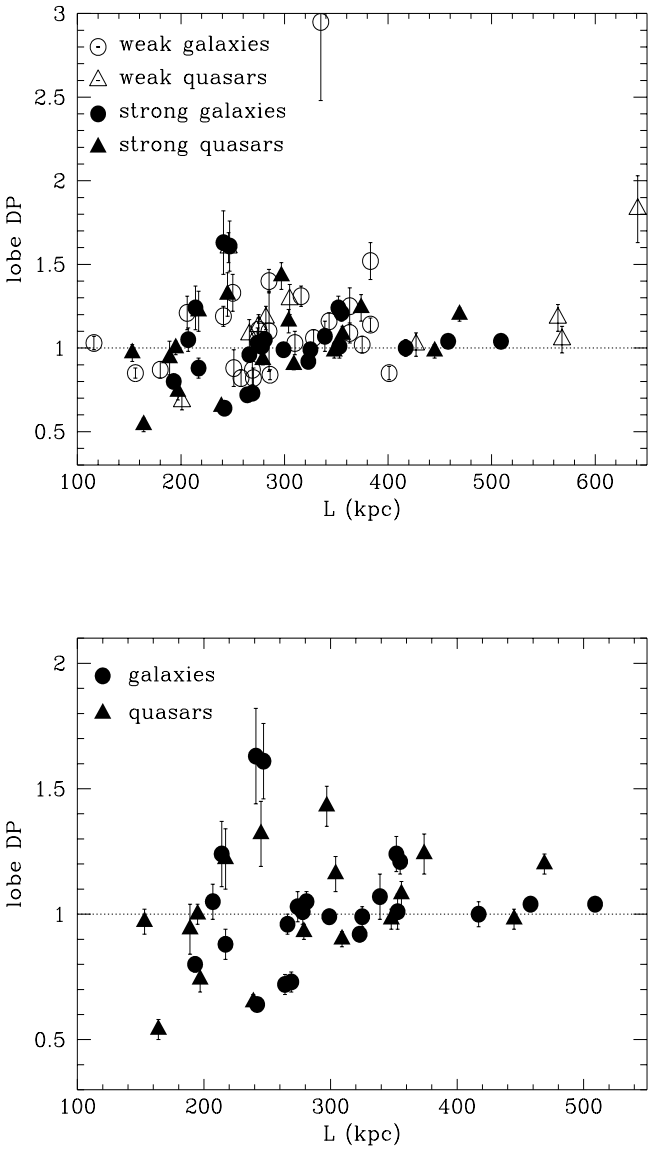

Figure 2. Depolarization of each lobe against its linear separation from the core or optical position for the entire sample (upper panel) and for the strong lobes (lower panel).

[t]

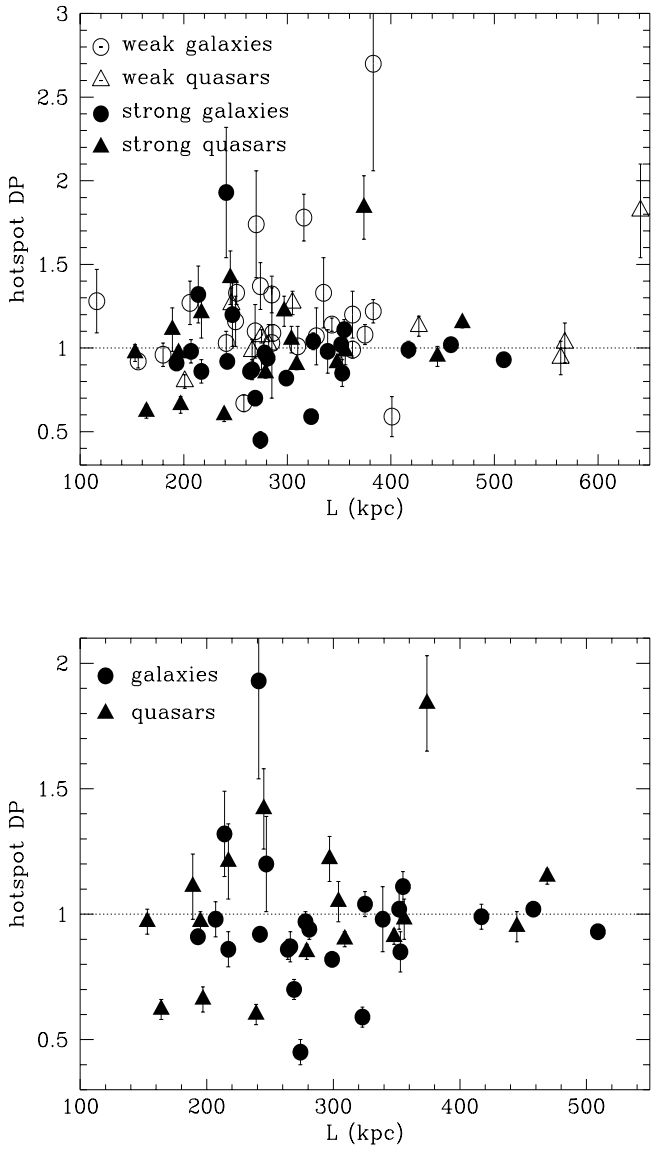

Figure 3. Depolarization of the hotspots against their linear separations from the core or optical position for the entire sample (upper panel) and for the sample of strong lobes (lower panel).

their emission-line properties which are being presently investigated.

In Figure 4 (upper panel) we plot for each lobe the ratio, r_θ (arm-length ratio), of its separation from the nucleus to that of the opposite lobe, against the depolarization parameter of the lobe. As we are plotting the DP for each lobe or hotspot with significant polarized flux density at λ20 and 6 cm, r_θ is < 1 for the nearer lobe or hotspot and > 1 for the farther one. There is a trend for the lobes with DP<1 to have r_θ <1, i.e. they are closer to the nucleus compared to the lobes on the opposite side. For the entire sample of 76 lobes, 20 of 39 with r_θ <1 have DP < 1, while of those with r_θ >1 this is true for only 7 of the 37 lobes. A Kolmogorov-Smirnov test shows that the DP distributions for sources with $r_\theta < 1$ is different from those with $r_\theta > 1$ at a significance level of > 99 per cent. Concentrating on the sample of strong lobes, DP < 1 for 15 out of 25 lobes with r_θ <1, but for only 3 out of 15 with r_θ >1. Among the eight lobes with significant depolarization, DP < 0.90, all are on the nearer side with r_θ <1. A similar trend is also seen for the

[t]

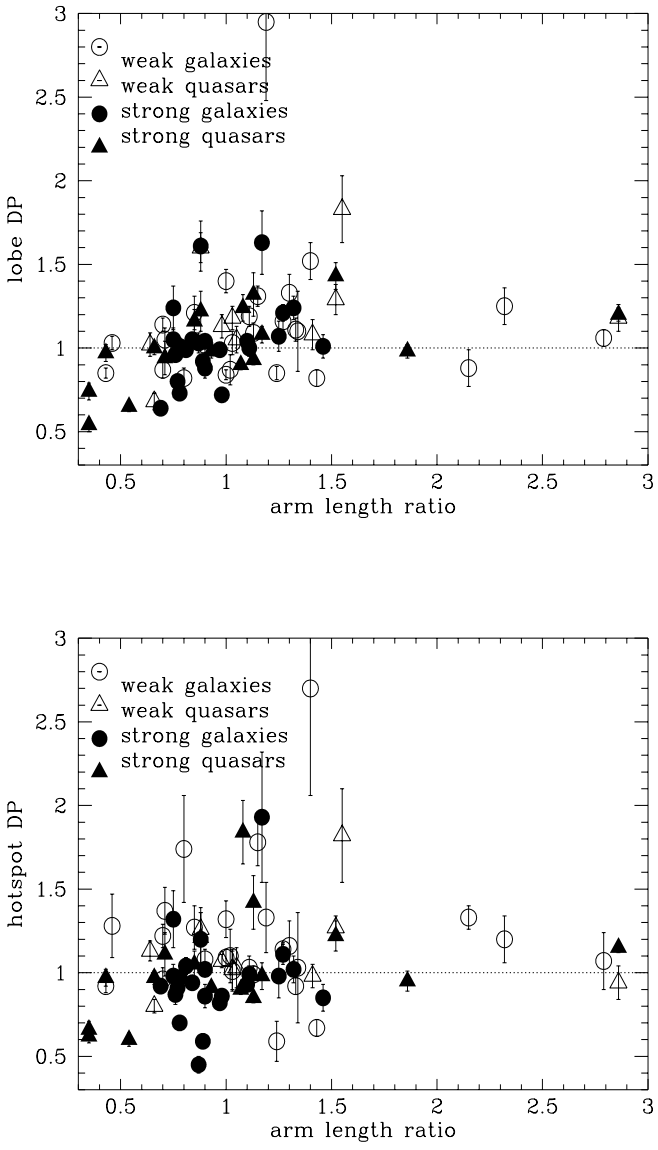

Figure 4. The depolarization of each lobe (upper panel) and hotspot (lower panel) against the arm-length ratio for the entire sample with filled points denoting the sample of strong lobes.

hotspots. There are 12 hotspots with DP < 0.9, 10 of which have r_θ <1.

The tendency for the shorter arm to be more depolarized can also be seen clearly if the arm-length ratio, defined to be the ratio of the length of the short arm to the length of the longer arm, is plotted against the depolarization of the short arm to the depolarization of the longer arm (Figure 5). It is seen that in 28 of the 35 sources, where the depolarization of the both the lobes have been determined, the nearer lobe is more depolarized than the farther one. There is a weak trend for the most asymmetric sources to have a lower depolarization ratio, similar to what was observed by Pedelty et al. (1989). This is seen more clearly in Figure 5 when one considers the galaxies and quasars with strong lobes. The dependence of depolarization ratio on arm-length ratio was studied by GCL91, but they did not find any such trend. Their sample consists largely of quasars with known radio jets and are of smaller angular size compared to our sources. In a sample of quasars selected to have known radio jets, the objects are likely to be close to the line of sight and effects of orientation should be dominant. The counter-jet side which exhibits significantly stronger depolarization is often farther from the nucleus. This is possibly due to intrinsic non-collinearities which may also appear amplified if the sources are at small angles to the line of sight. In our sample the sources are of large angular and linear size, reasonably collinear and the observed trend is possibly due to an asymmetric environment as well as effects of orientation. Comparison of the depolarization information with narrow-band images, and detection of radio jets in these objects should help clarify the situation.

4.3 Flux density and brightness ratio of the lobes

However, an examination of the brightness asymmetry of the lobes and its relationship to the arm-length asymmetry might also provide us with valuable insights. For example, if the source and the environment are intrinsically symmetric, the approaching component would be farther from the nucleus and brighter due to relativistic enhancement of the hot-spot flux density, provided the effects of evolution of individual components with age over the length scales of our sources are not signficant (Ryle & Longair 1967; Swarup & Banhatti 1981). On the other hand, if the source is evolving in an asymmetric environment, there will be a greater dissipation of energy on the side with the higher density which will also be closer to the nucleus (Eilek & Shore 1989; Gopalkrishna & Wiita 1991). Figure 6 shows the arm-length ratio, defined to be ≤1, plotted against the peak brightness ratio, which is the ratio of peak brightness of the nearer lobe to the farther one. There is a clear trend for the nearer component to be brighter, so that the ratio is >1 in 29 of the 41 objects in the sample. This is particularly true for the more asymmetric sources, say r_θ <0.8, where 18 of the 22 sources have the brighter component closer to the nucleus. A similar trend is also seen while considering the total flux density ratio of the lobes. The sample of 3CR sources studied by McCarthy et al. (1991) shows a similar but weaker trend. This trend in our sample suggests that an asymmetric environment on opposite sides of the nucleus affects the flux density and arm-length ratios of the lobes, in addition to the observed depolarization asymmetry of the oppositely-directed lobes.

4.4 Depolarization Asymmetry

In the unified scheme for radio galaxies and quasars, the quasars are inclined at smaller angles to the line of sight. If the depolarization is caused by a magnetioionic halo associated with the parent optical object or a cluster of galaxies associated with it, the pathlength difference for the radiation from the two oppositely-directed lobes will be larger

[t]

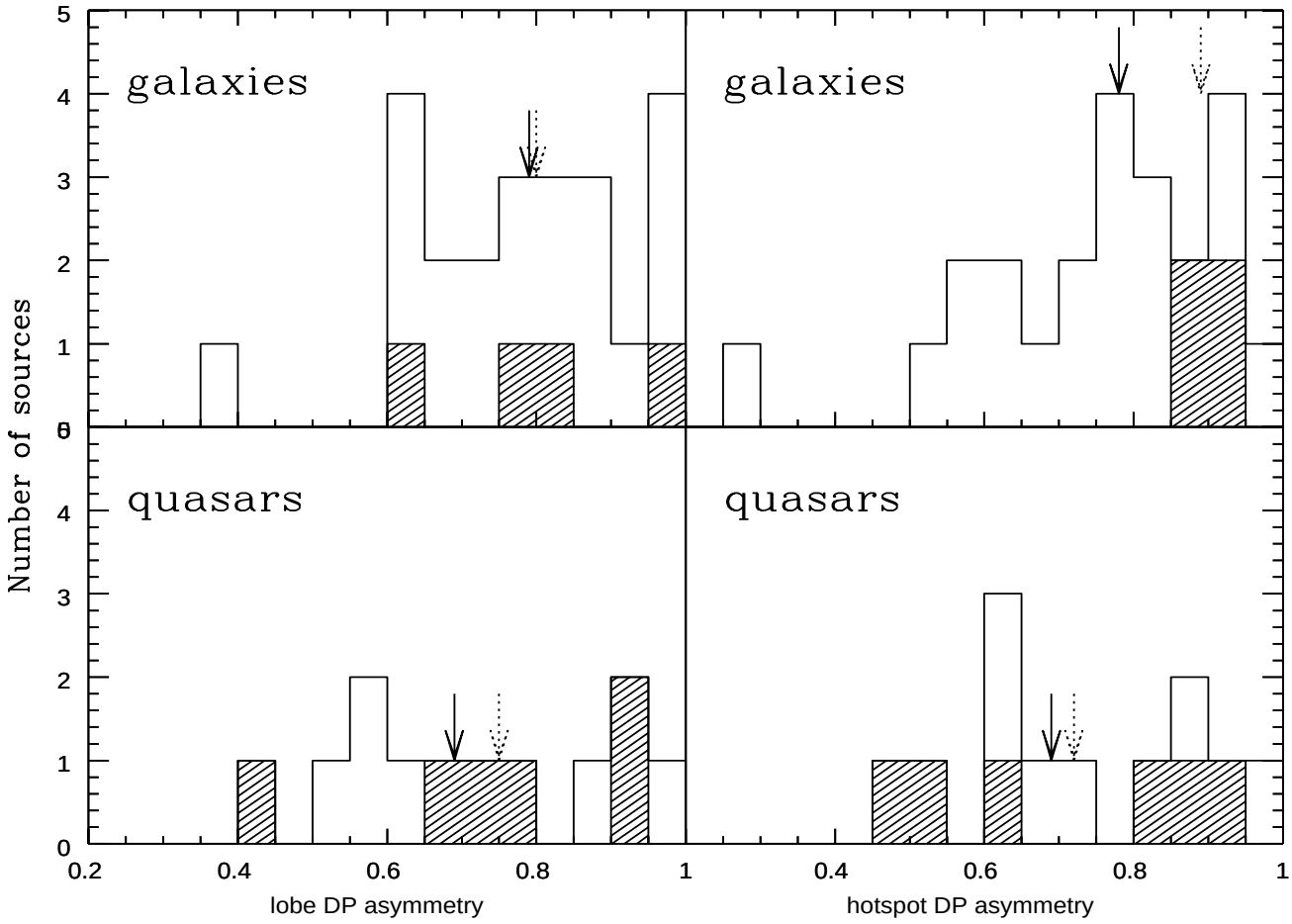

Figure 7. The distributions of the ratio of depolarization of the lobes (left panel) and hotspots (right panel) on opposite sides of the parent galaxy. The ratio is defined to be $\leq$1, and is shown shaded for the sample of strong lobes. The solid and dotted arrows show the median values for the entire sample and the sample of strong lobes respectively.

for quasars compared to the galaxies. Hence the quasars should exhibit a higher degree of depolarization asymmetry of the lobes or hotspots compared to the galaxies. We can attempt to infer an average statistical angle of inclination to the line of sight for our sample of galaxies and quasars using the fraction of emission from the core as a statistical indicator of orientation to the line of sight. All the quasars in our sample have detected radio cores, with the median fraction of emission from the core at an emitted frequency of 8 GHz being about 12%. Most of the galaxies do not have detected cores, and the upper limit is generally less than about 0.1%. Assuming that the intrinsic fraction of emission from the nucleus is similar to that of 3CR sources (cf. Saikia & Kulkarni 1994), the core strength of galaxies and quasars are consistent with angles of inclination of about 65° and 30° respectively. The expected depolarization asymmetry between λ20 and 6 cm for our sources using the typical parameters listed by GCL91 are close to about 1 and 0.8 for the galaxies and quasars respectively. However, our sources are much larger than those in GCL91, and we need to determine more reliably the parameters for the environment on these scales using X-ray and optical observations along with long-wavelength radio polarization measurements.

Since we do not detect jets in almost all but one of our sources we examine the DP asymmetry for both radio galaxies and quasars, bearing in mind that the trend could be diluted by intrinsic asymmetries in the environment. In Figure 7, we present the depolarization asymmetry for both radio galaxies and quasars using the depolarization values for both the lobes and hotpots. We define the depolarization asymmetry as the ratio of the depolarization of one lobe to the other such that the ratio is always less than 1. There is a marginal trend for the quasars to be more asymmetric, consistent with the sense expected in the unified scheme. The median values for the entire sample of galaxies and quasars are about 0.78 and 0.67 respectively for the lobes as well as the hotspots. Considering the lobes and hotspots from the sample of strong sources, the median values of DP asymmetry of the lobes are 0.80 and 0.75 for the galaxies and quasars respectively, while the corresponding values for the hotspots are 0.89 and 0.72 respectively. Since the environments are likely to be asymmetric, as discussed earlier, and

[t]

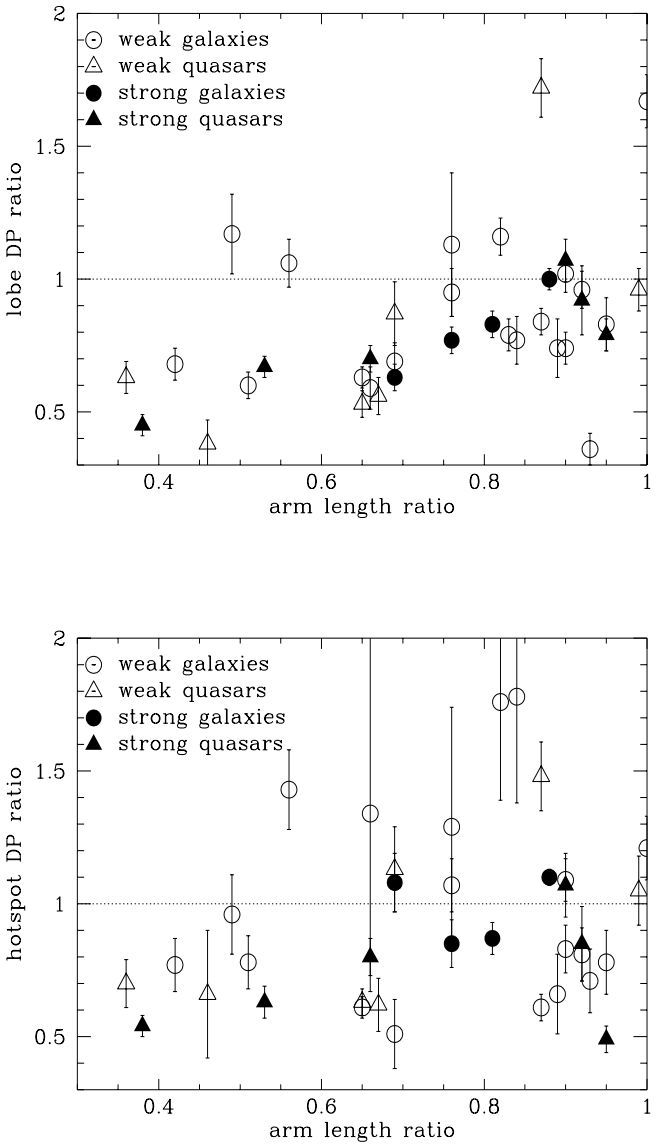

Figure 5. The depolarization of the nearer lobe (upper panel) or hotspot (lower panel) to the farther one for each source against the arm-length ratio, which is now defined to be always $\leq$1. The sample of strong lobes is denoted by the filled points.

the sources are large, the effects of orientation are seen as a marginal trend.

4.5 Laing-Garrington effect

In the Laing-Garrington effect the counter-jet side depolarises more rapidly due to the extra pathlength through the magnetoionic medium. In our sample we detect a radio jet in only one object, namely the quasar 0454−220. The depolarization value for the lobe and the hotspot on the counter-jet side is 0.65± 0.03 and 0.60± 0.04 and for the jet side these values are 0.98± 0.04 and 0.95± 0.04 respectively. This is clearly consistent with the Laing-Garrington effect. The arm-length ratio, r_θ defined to be <1, is 0.53 with the counter-jet lobe being the nearer one, while the DP ratio of this lobe to the farther one is 0.67 ± 0.04 and 0.63 ± 0.06 for the hotspot. The component on the jet side is brighter, possibly due to mild relativistic beaming of the hotspot. In this case, since we can unambiguously identify the approaching component assuming the jet asymmetry to be due to relativistic beaming, the tendency for r_θ and DP to be <1, is largely due to the extra pathlength of the receding lobe. It is important to try and detect radio jets in a larger number of these objects to assess the relative importance of orientation and environmental effects.

[t]

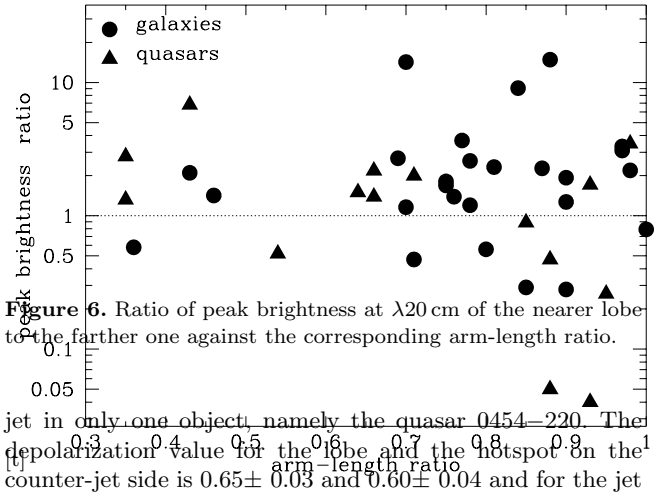

Figure 6. Ratio of peak brightness at λ20 cm of the nearer lobe to the farther one against the corresponding arm-length ratio.

5 CONCLUDING REMARKS

We have investigated the effects of environment and orientation on the observed depolarization properties of a sample of high-luminosity radio galaxies and quasars between λ 20 and 6 cm. We find that significant depolarization is usually seen in the lobes which are within about 300 kpc of the parent galaxy. Among the 17 lobes in the entire sample which show significant depolarization with DP<0.9, 15 are within 300 kpc from the parent galaxy. Comparing the depolarization on opposite sides of the source, we find that the side which is closer to the parent galaxy shows significant depolarization. Of these 17 lobes where significant depolarization is seen, 13 of them are closer to the parent galaxy compared to the lobe on the opposite side. The ratio of the depolarization parameter of the nearer lobe to the farther one is <1 for 28 of the 35 sources in the entire sample with reliable polarization information for both lobes. The nearer component is also brighter in 26 of these 35 objects, suggesting that the nearer component is advancing outwards through a denser environment which is responsible for stronger depolarization and greater dissipation of energy. The depolarization

asymmetry of the lobes on opposite sides for galaxies and quasars shows that the latter are marginally more asymmetric, consistent with the trend expected in the unified scheme. In our sample of sources the polarization properties of the lobes appear to be due to an asymmetric environment on opposite sides of the parent optical object, as well as possibly due to different orientations of the sources to the line of sight. Detailed information on the distribution of the depolarizing medium from optical and X-ray observations, as well as detection of radio jets in these objects to identify the approaching and receding components, should enable us the clarify better the relative importance of the effects of an asymmetric environment and orientation.

Acknowledgements

The National Radio Astronomy Observatory is a facility of the National Science Foundation operated under cooperative agreement by Associated Universities Inc. We thank the staff of the Very Large Array for the observations, and Gopal-Krishna and A. Pramesh Rao for their comments on the manuscript.

REFERENCES

Antonucci R., 1993, ARA&A, 31, 473
Baars J.W.M., Genzel R., Pauliny-Toth I.I.K., Witzel A., 1977, A&A, 61, 99
Barthel P. D., 1989, ApJ, 336, 606
Burn B. J., 1966, MNRAS, 133, 67
Chiu Y. T., 1975, Journ. Atmosph. Terr. Phys., 37, 1563
Dennett-Thorpe J., Bridle A. H., Scheuer P. A. G., Laing R. A., Leahy J. P., 1997, MNRAS, 289, 753
Eilek J.A., Shore S.N. 1989, ApJ, 342, 187
Fanaroff B. L., Riley J. M., 1974, MNRAS, 167, 31p
Garrington S. T. Leahy J. P., Conway R. G., Laing R. A., 1988, Nature, 331, 147
Garrington S. T., Conway R. G., Leahy J. P., 1991, MNRAS, 250, 171 (GCL91)
Garrington S. T., Conway R. G., 1991, MNRAS, 250, 198
Gopal-Krishna, Wiita P.J., 1991, ApJ, 373, 325
Holmes G.F. 1991, PhD Thesis, University of Manchester
Jägers W. 1986, PhD Thesis, University of Leiden
Johnson R. A., leahy J. P., Garrington S. T., 1995, MNRAS, 273, 877
Kapahi et al. 1998a, ApJS, in press
Kapahi et al. 1998b, ApJS, in press
Laing R. A., 1988, Nature, 331, 149
Laing R.A., 1993, in Astrophysical Jets, eds: Burgarella, D. Livio, M., O'Dea C., Cambridge Univ. Press, p 95
Large M. I., Mills B. Y., Little A. G., Crawford D. F., Sutton J. M., 1981, MNRAS, 194, 693
Liu R., Pooley G., MNRAS, 1991, 253, 669
McCarthy P.J., Kapahi V.K., van Breugel W., Persson S.E., Athreya R.M., Subrahmanya C.R., 1996, ApJS, 107, 19
McCarthy P. J., van Breugel W., Kapahi V. K., 1991, ApJ, 371, 478
Parma P., Morganti R., Capetti A., Fanti R., de-Ruiter H. R., 1993, A&A, 267, 31
Pedelty J. A., Rudnick L., McCarthy P. J., Spinrad H., 1989 AJ, 97, 647
Perley R.A., 1996, VLA Calibrator Manual, NRAO.
Ryle M., Longair M.S., 1967, MNRAS, 136, 123
Saikia D.J., 1981, MNRAS, 197, 11P
Saikia D.J., Kulkarni V.K., 1994, MNRAS, 270, 897
Saikia D. J., Salter C. J., 1988, ARA&A, 26, 93
Saikia D.J., Garrington S.T., Holmes G.F. 1997. Quasar Hosts : ESO Astrophysics Symposia, eds Clements D.L., Pérez-Fournon I., Springer, p. 13
Swarup G., Banhatti D.G., 1981, MNRAS, 194, 1025
Strom, R. G., Jägers, W. J., 1988, A&A, 194, 79
Thompson A. R., Clark B. G., Wade C. M., Napier P. J., 1980, ApJS, 44, 151
Urry C. M., Padovani P., 1995, PASP, 107, 803